Some things old, new and borrowed: Delivery of dabrafenib and vemurafenib to melanoma cells via self-assembled nanomicelles based on an amphiphilic dendrimer

Maria Russi [a], Rachele Valeri [a], Domenico Marson [a], Chiara Danielli [b], Fulvia Felluga [b], Aura Tintaru [c], Natasa Skoko [d], Suzana Aulic [a,d], Erik Laurini [a,*], Sabrina Pricl [a,e]

[a] Molecular Biology and Nanotechnology Laboratory (MolBNL@UniTS) – DEA, University of Trieste, Piazzale Europa 1, Trieste 34127, Italy
[b] Department of Chemical and Pharmaceutical Sciences, DSCF, University of Trieste, Via Giorgeri 1, Trieste 34127, Italy
[c] Aix Marseille Univ, CNRS - Centre Interdisciplinaire de Nanosciences de Marseille (CINaM) UMR 7325 - Département IMMF - Campus Luminy, 163, Avenue de Luminy, Marseille 13288, France
[d] Biotechnology Development Unit, International Centre for Genetic Engineering and Biotechnology (ICGEB), Trieste, Italy
[e] Department of General Biophysics, University of Łódź, ul. Pomorska 141/143, Łódź 90-236, Poland

ARTICLE INFO

ABSTRACT

Two clinically approved anticancer drugs targeting BRAF in melanoma patients – dabrafenib (DAB) and vemurafenib (VEM) – have been successfully encapsulated into nanomicelles formed upon self-assembly of an amphiphilic dendrimer AD based on two C_{18} aliphatic chains and a G2 PAMAM head. The process resulted in the formation of well-defined (~10 nm) core-shell nanomicelles (NMs) with excellent encapsulation efficiency (~70% for DAB and ~60% for VEM) and good drug loading capacity (~27% and ~24% for DAB and VEM, respectively). Dynamic light scattering (DLS), transmission electron microscopy (TEM), small-angle x-ray scattering (SAXS), nuclear magnetic resonance (NMR), isothermal titration calorimetry (ITC), and molecular simulation (MS) experiments were used, respectively, to determine the size and structure of the empty and drug-loaded nanomicelles (DLNMs), along with the interactions between the NMs and their cargoes. The *in vitro* release data revealed profiles governed by Fickian diffusion; moreover, for both anticancer molecules, an acidic environment (pH = 5.0) facilitated drug release with respect to physiological pH conditions (pH = 7.4). Finally, both DAB- and VEM-loaded NMs elicited enhanced response with respect to free drug treatments in 4 different melanoma cell lines.

1. Introduction

Melanoma is a highly aggressive type of cancer that affects the integumentary system and for which a family history of the disease, a fair complexion, the presence of a large number of moles, and skin exposure to natural/artificial ultraviolet (UV) radiation constitute established risk factors for malignancy development. The most recent epidemiological assessment of global cancer data (Arnold et al., 2022) estimates that 325,000 new melanoma cases and 57,000 deaths due to this tumor occurred in 2020, with large geographic variations in incidence across countries and world regions. Should the 2020 rates remain stable, according to the same report the global burden from melanoma is estimated to increase to 510,000 new cases and 96,000 deaths by 2040.

In the last ten years, however, a significant progress in the knowledge of the major oncogenes and signaling pathways involved in the growth of melanoma has been achieved; this, in turn, has opened new avenues to the development of novel therapeutic approaches.

The v-RAF murine sarcoma viral oncogene homolog B1 (BRAF) is a serine/threonine protein kinase that plays a critical role in the RAS-RAF-MEK-ERK mitogen–activated protein kinase (MAPK) cell signaling pathway. Despite over 20 years of research into the regulation and function of the RAF proteins, it was only realized recently that the BRAF isoform is mutated at a high frequency in different human cancers, identifying this kinase as another important oncogene along this pathway (Garnett and Marais, 2004). Focusing on melanoma, activating BRAF mutations were identified in 37%−53% of patients with the

* Corresponding author.
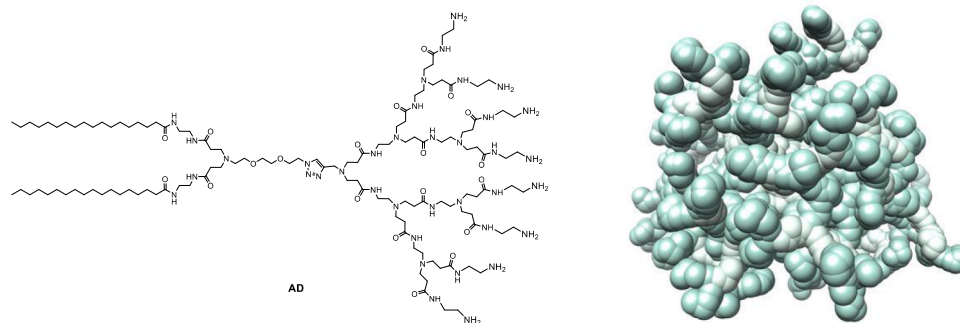*E-mail address:* erik.laurini@dia.units.it (E. Laurini).

Fig. 1. (Left) Chemical structure of the amphiphilic dendrimer AD. (Right) Molecular model of a nanomicelle formed by AD upon self-assembly.

malignant form of this pathology, the most prevalent, missense kinase alteration being the replacement of the small, apolar residue valine (V) with the negatively-charged, phosphorylation mimicking glutamic acid (E) at position 600 (BRAF^{V600E}) within the protein catalytic (*i.e.*, ATP binding) site (Cantwell-Dorris et al., 2011). It is interesting to note that BRAF^{V600E} is not a UV-driven mutation; in fact, it may also be found in the molecular profile of atypical benign nevi; moreover, although BRAF^{V600E} is the most frequent mutation (accounting for nearly 40% of all melanomas and in approximately 90% of BRAF-mutant melanomas), other more or less frequent activating variants in BRAF have also been reported, which include other aminoacidic substitutions at the same position (*e.g.*, V600K/D/R), G469A/V/S, L597Q/R/S/V, and K601E/N/T, among others (Dankner et al., 2018). The milestone discovery that melanoma cells can undergo cell cycle arrest and subsequent apoptosis when mutant BRAF proteins are selectively inhibited by small-molecule ligands generated a paradigm shift in the management of metastatic and/or unresectable melanoma carrying BRAF mutated isoforms (Holderfield et al., 2014; Ribas and Flaherty, 2011). Accordingly, in 2011 the American Food and Drug Administration (FDA) – followed 1 year later by the European Medicines Agency (EMA) – authorized the use of vemurafenib (VEM) (aka PLX4032 or Zelboraf®) as the first selective BRAF^{V600E} inhibitor for melanoma based on the relevant clinical outcomes (Bollag et al., 2012; Tsai et al., 2008). The current portfolio of BRAF inhibitors (BRAFis) approved for melanoma treatment includes, besides VEM, dabrafenib (DAB, Tafinlar®) (Rheault et al., 2013) and encorafenib (ENC) (Carr et al., 2020; Koelblinger et al., 2018); all three BRAFis nest within the ATP-binding pocket of the active conformation of the kinase, with enhanced affinity for the BRAF^{V600E} isoform, ultimately resulting in improved potency and specificity (Roskoski, 2018). Most importantly, clinical studies based on these BRAFis monotherapies for metastatic melanoma demonstrated a high objective response (OR) rate and enhanced overall survival (OS) compared to conventional chemotherapy (Chapman et al., 2011, 2017; Hauschild et al., 2012). Combining BRAFis with MEK inhibitors (MEKis) such as cobimetinib (Cotellic®), trametinib (Mekinist®), and binimetinib (Mektovi®) resulted with additional therapeutic advantages, including further improvement in OR rates and OS (Dummer et al., 2018; Hamid et al., 2019; Robert et al., 2019; Roskoski, 2018). On the negative side, all BRAFis administration comes with several side effects, including arthralgia (joint pain), diarrhea, fatigue, nausea, and skin rash along with the generation of keratoacanthomas (*i.e.*, well-differentiated, low-grade and rapidly growing squamous cell skin carcinomas). These tumors are readily identified, simple to excise, and not metastatic. However, the development of such tumors is clearly an undesired outcome. Moreover, DAB is prone to cause fever [34] while VEM is

associated with photosensitivity. Most importantly, however, almost all of the patients who are treated with single-agent BRAFis or with BRAFi/MEKi combinations ultimately acquire resistance to the treatment and undergo disease relapse (Haugh et al., 2021; Lito et al., 2013; Rossi et al., 2019; Tangella et al., 2021; Tian and Guo, 2020).
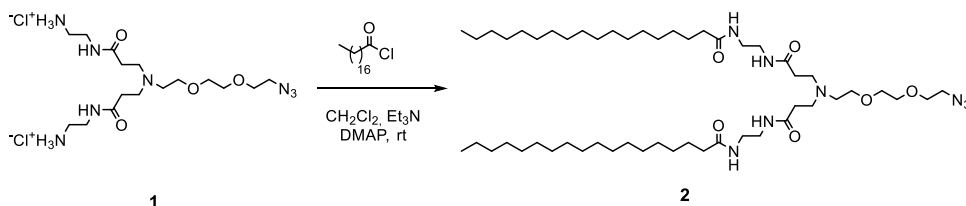
Oral BRAFis administration is undoubtedly the most convenient for patients; however, this method requires the drug to traverse the acidic environment of the stomach. Many active compounds are denatured or degraded by stomach acid, and even if a drug survive this harsh situation, it must next overcome the intestinal mucus barrier to reach its target. Some medicines, particularly hydrophobic ones, may be readily get trapped by mucus and, as a result, are rapidly eliminated before they can be absorbed by the gut. Bioavailability of oral drugs can also be less than 100% for any of the following reasons: oral medications are absorbed and distributed more slowly than intravenous (IV)-delivered drugs; the quantity of medicine absorbed may depend on the condition of the gastrointestinal (GI) tract (*e.g.*, presence of food, intestinal health/integrity, GI tract speed, etc.), and enzymes located everywhere in the GI system may degrade oral medications. Also, given that oral medication absorption is slower than the adsorption achieved *via* systemic administration, and that oral drugs take longer to reach the bloodstream, drug clearance will also likely take longer, resulting in enhanced side effects. Under this perspective, it may be highly beneficial to deliver hydrophobic medications intravenously with the help of nanovectors by taking advantage of the leaky angiogenic tumor vasculature and its compromised lymphatic drainage (a phenomenon known as the enhanced permeability and retention effect, or EPR). In fact, compared to low molecular weight molecules that disperse widely throughout the body, the absorption and retention of a stable drug-loaded nanocarrier through extravasation from the circulation to the tumor tissue may be higher. As an example, Pisarevsky et al. recently proposed a poly(α,L-glutamic acid) (PGA) covalently modified withy dabrafenib and selumetinib (a MEKi) as a parenterally-delivered nanosystem able to inhibit melanoma proliferation more efficiently than the two free drugs both *in vitro* and *in vivo* (Pisarevsky et al., 2020).

To bypass patient's discomfort due to IV treatments, topical delivery offers a valid alternative for the treatment of numerous skin conditions, including skin cancers. This is significant since the therapy is limited to the afflicted skin region and presents negligible systemic toxicity. In particular, in recent years microneedles (MNs) – that is arrays of tiny projections on a solid support that are minimally invasive, painless devices able to penetrate the *Stratum corneum* and epidermal skin barriers – allowed delivery of medicines that ordinarily would not be delivered into or across the skin. Indeed, several forms of MNs, including dissolved, solid, hollow, and coated MNs, have been utilized to treat skin

malignancies including melanoma, squamous cell carcinoma, and basal cell carcinoma (Zhi et al., 2021). In particular, such systems have been used recently in the nanovector-assisted MN-based transdermal delivery of a variety of nucleic acids (including oligonucleotides, small interfering RNAs (siRNAs), and plasmid DNA (pDNA)) and drugs or biologics (including, *e.g.,* cisplatin, curcumin, doxorubicin and 5-fluorouracil, peptides and antibodies) into the skin tissue, providing broad application prospects for cancer therapy, particularly in the treatment of melanoma (Lee et al., 2020; Wang et al., 2016).

Therefore, with the goal of reducing the major side effects and enhance the effectiveness of BRAFis, we performed a preliminary investigation about the possibility of delivering DAB and VEM to melanoma cells utilizing a nanocarrier as a proof-of-concept. If successful, this technique could be further expanded to BRAFi/MEKi codelivery either *via* systemic or MN-assisted administration. To the purpose, we exploited the ability of our amphiphilic dendrimer AD, composed by two C_{18} lipid-like chains and a poly(amidoamine) (PAMAM) dendron head (Fig. 1, left) to self-assemble into small nanomicelles (NMs, Fig. 1, right) and to effectively deliver different cargoes (*e.g.,* siRNA or doxorubicin) to different tumors both *in vitro* and *in vivo* (Dong et al., 2018b; Ellert-Miklaszewska et al., 2019; Liu et al., 2014; Wei et al., 2015; Laurini et al., 2021a).

In the case of small drug encapsulation and delivery in particular, we already verified that the small NMs formed by AD are endowed with high drug loading, fast and efficient cellular uptake *via* the micropinocytosis pathway, and effective enhancement of drug anticancer activity due to preferential accumulation at tumor site, along with an ensuing reduction of systemic toxicity in a preclinical model of breast

2. Materials and methods

2.1. Synthesis of the amphiphilic dendrimer AD

2.1.1. General information

Commercial reagents and solvents were purchased from Sigma-Aldrich. Column flash chromatography was run on silica gel 60 (230−400 mesh). Reactions were monitored by thin-layer chromatography on silica gel plates using UV light as the visualizing and $KMnO_4$ as the developing agent. Click chemistry reaction was carried out in an Anton Parr Microwave 400 Synthesis Reactor. Centrifugation was performed in a Neya 8 Bench Top Centrifuge. Dialysis of AD was run in water with the use of benzoylated dialysis tubing (Sigma-Aldrich), flat width 32 mm, MWCO 2000. NMR spectra were recorded on a Varian 500 MHz spectrometer at 500 MHz (^{1}H) and 125 MHz (^{13}C), and on a Varian 400 MHz spectrometer at 400 MHz (^{1}H) and 100 MHz (^{13}C). Chemical shifts are in ppm (δ) with $CDCl_3$ ($\delta = 7.26$ for ^{1}H NMR and 77.0 for ^{13}C NMR) or with MeOD ($\delta = 3.34$ for ^{1}H NMR and 47.60 for ^{13}C NMR) used as reference. Coupling constants J are given in Hertz. ^{1}H and ^{13}C NMR resonances were assigned using a combination of distortionless enhancement by polarization transfer (DEPT), correlation spectroscopy (COZY), and heteronuclear single quantum coherence (HSQC) spectra. Electrospray (ESI) mass spectra were obtained on a Bruker Daltonics Esquire 4000 spectrometer. ESI-TOF (time-of-flight) mass spectra were recorded on a Bruker micrOTOF-Q spectrometer. Compound yields refer to spectroscopically (^{1}H NMR) homogeneous materials.

2.1.2. Synthesis of the azide 2

1   **2**

cancer (Wei et al., 2015). The choice of these AD nanocarriers, instead of other nanovector systems, also derived from their ability to spontaneously self-assemble into supramolecular entities promoting a simpler and more effective synthetic approach. Furthermore, AD nanomicelles have already exhibited low toxicity profiles both *in vitro* (by MTT and lactate dehydrogenase assays and by testing their haemolytic activity) and *in vivo* (Liu et al., 2014; Wei et al., 2015; Laurini et al., 2021a). Finally, given the excellent results achieved in the delivery of doxorubicin, we found stimulating to test the efficiency of ADs in encapsulating drugs with a structure and chemical / physical properties different from the classic antineoplastic molecule. In the light of these evidences, we decided to investigate the possibility of using AD NMs to encapsulate and deliver the two clinically approved BRAFis DAB and VEM using both *in silico* and *in vitro* models. To the purpose, in this work we firstly propose a revise and more effective synthetic protocol to the obtainment of the AD amphiphile, then we present a characterization of the empty and drug-loaded AD NMs based on a number of different experimental and computational techniques, and finally report the results from *in vitro* tests of their anticancer activity in a panel of 4 different melanoma cell lines.

In a three-necked 100 mL round bottomed flask, a 20 mL CH_2Cl_2 solution of the diamine 1·2HCl, (2.0 g, 5.0 mmol), prepared according to the procedure described by Budin and coworkers (Budin et al., 2010) and Et_3N (2.5 mL), was cooled to 0 °C. Steaoryl chloride (3.76 g, 12.5 mmol) and a catalytic amount of DMAP (N,N-dimethylaminopyridine), dissolved in 10 mL CH_2Cl_2, were added under Ar, leading to the immediate formation of a white precipitate. The suspension was left on stirring at room temperature (rt) overnight, then CH_2Cl_2 was evaporated under reduced pressure leaving a foamy solid-like material that was dispersed in water and collected by centrifugation (5000 rpm, 15 min, rt). The procedure was repeated 3 times to completely remove $Et_3N·HCl$, discarding the aqueous supernatant solution. The final residue was dissolved in CH_2Cl_2 and the solution dried over Na_2SO_4. Evaporation of the solvent left compound 2 in 81% yield (3.78 g), that was used in the next step without further purification. ^{1}H NMR (400 MHz, $CDCl_3/CD_3OD$ 5:1) δ 3.82–3.81 (m, 6H, 3 x CH_2O), 3.68 - 3.64 (m, 8H, 4 x C$\underline{H}_2$NHCO), 3.59 (t, 2H, CH_2O), 3.41 (t, 2H, CH_2N_3), 2.82 (br, 4H, 2 x CH_2N), 2.72 (br, 2H, CH_2N), 2.36 (m, 4H, 2 x CH_2CONH), 2.17 (t, 4H, -$(CH_2)_{16}$C$\underline{H}_2$CO), 1.59 (m, 4H, -$(CH_2)_{15}$C$\underline{H}_2$CH$_2$CO), 1.28–1.25 (m and s, 56H, 28 x CH_2), 0.88 (t, 6H, 2 x C$\underline{H}_3$CH$_2$) ppm; ^{13}C NMR (100 MHz, $CDCl_3/CD_3OD$ 5:1) δ 175.1, 173.8, 70.6, 70.40, 70.45, 68.75 (CH_2N_3),

52.9, 50.7, 50.35, 39.5, 39.0, 36.6, 33.4, 32.0, 29.8–29.5, 25.9, 25.9, 22.75, 14.1 ppm. ESI-MS: 935.9 $[M + H]^+$; 957.7 $[M+Na]^+$ (Figure S1).
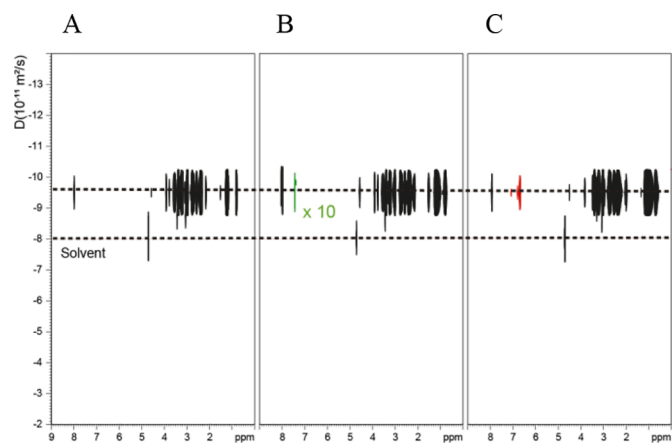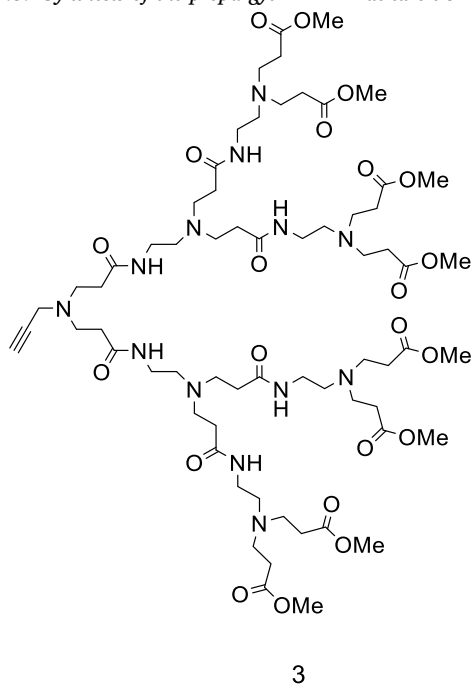
2.1.3. Synthesis of the propargyl-PAMAM dendron 3

3

Fig. 3. ^{1}H-DOSY spectra of AD (A), VEM/AD (B) and DAB/AD (C) nanomicelles obtained in D_2O at 500.13 MHz and 300 K. For clarity, the intensity of the VEM distinctive signal (green) was increased 10 times while the distinctive signals of DAB are shown in red. (For interpretation of the references to colour in this figure legend, the reader is referred to the web version of this article.).

Dendron 3 was synthetized as described by Lee et al. (Lee et al., 2006), starting from propargylamine (0.44 g, 0.52 mL, 8.0 mmol) by successive Michael additions of the primary amines to methyl acrylate and aminolysis of methyl ester groups with a large molar excess of ethylenediamine. All the ester and amine intermediates were directly used in the successive steps without purification, while the final
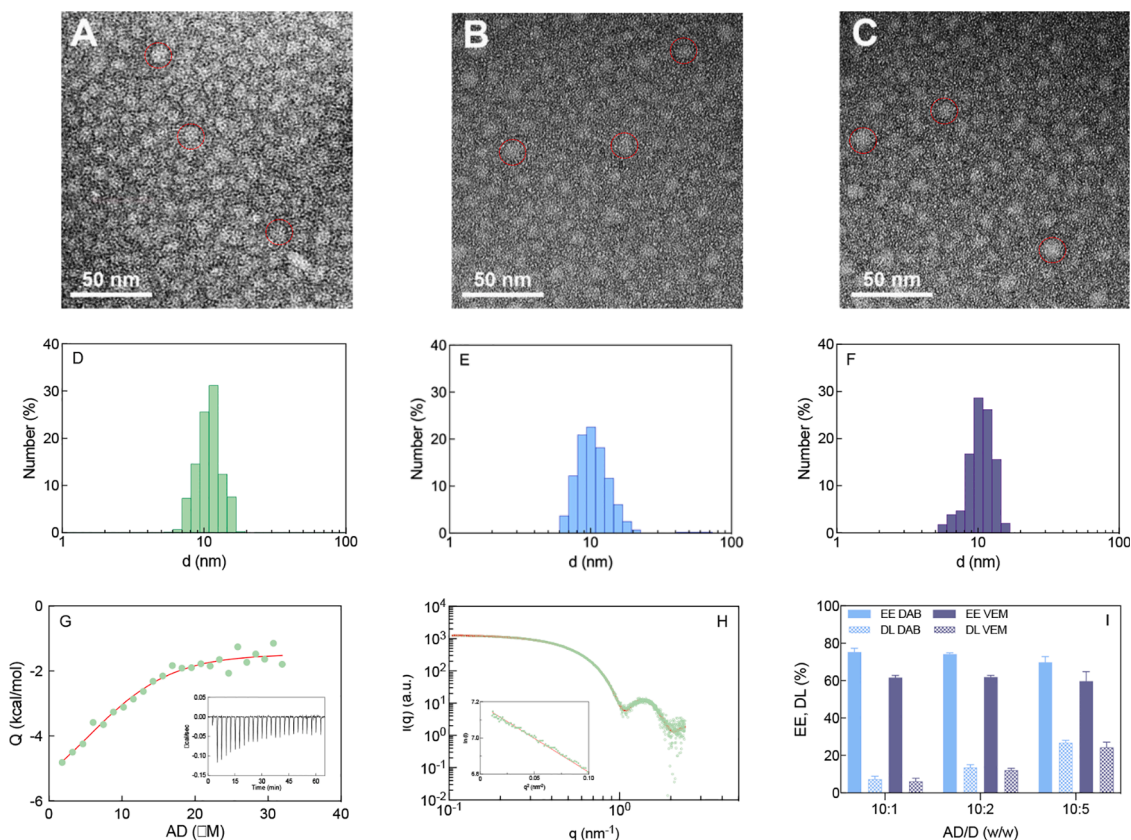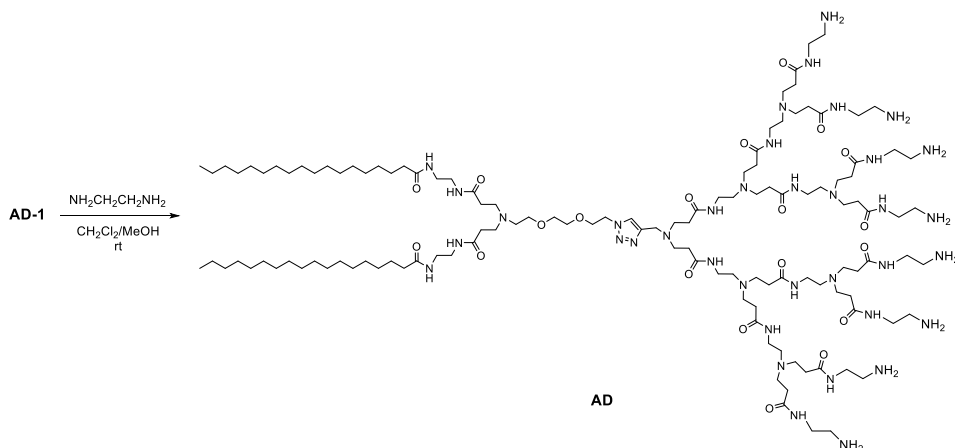

Fig. 2. (Top) TEM images of AD (A), DAB/AD (B), and VEM/AD (C) NMs. Red circles highlight three representative nanomicelles structure in each TEM ensemble. (Center) Hydrodynamic radius (R_h) of AD (D), DAB/AD (E), and VEM/AD (F) NMs at 25 °C as measured by DLS. (Bottom) (G) Representative integrated experimental ITC profiles (circles) and data fitting with a sigmoidal function (red line) for the demicellization process of AD in milliQ water. The insert shows the corresponding ITC raw data. (H) Experimental SAXS curve of AD NMs (circles) with the core-shell triaxial ellipsoid fitting (red line). The insert shows the Guinier plot of the NMs (circles) with the linear fit of data (red line). (I) Effect of different AD/drug weight ratio (AD/D) on the encapsulation performance of the NMs. EE = encapsulation efficiency (Eq. (1)); DL = drug loading (Eq. (2)).

octaester 3 was purified by flash chromatography (eluent: CH$_3$OH/E-tOAc gradient from 2% to 20%), after which it was isolated in a 67% total yield (7.64 g). ^{1}H and ^{13}C NMR data in agreement with those reported by Lee and coworkers (Lee et al., 2006). ^{1}H NMR (500 MHz, CDCl$_3$) δ 7.71 (bt, J = 5.0 Hz, 2H, 2 x NHCO), 7.08 (t, J = 5.4 Hz, 4H, 4 x NHCO), 3.67 (s, 24 H, 8 x OCH$_3$), 3.45 (d, J = 2.1 Hz, 2H, NCH$_2$C≡CH), 3.28 (m, 12H, 6 x CH$_2$NHCO), 2.80 (m, 12H, 6 x CH$_2$N), 2.75 (t, J = 6.7 Hz, 16H, 8 x CH$_2$N), 2.54 (bt, J = 6.0 Hz, 4H, 2 x CH$_2$N), 2.49 (t, J = 6.0 Hz, 8H, 4 x CH$_2$CO), 2.37 (q, J = 6.6 Hz, 16H, 8 x CH$_2$CO), 2.32 (t, 8H, 4 x CH$_2$CO), 2.21 (t, J = 2.2 Hz, 1H, C≡CH) ppm. ^{13}C NMR (125 MHz, CDCl$_3$) δ 173.0, 172.3, 172.1, 78.0, 73.5, 52.9, 52.5, 51.6, 49.8, 49.2, 41.0, 37.3, 37.1, 33.7, 32.6 ppm. ESI-MS: 1429.0 [$M + H$]$^+$; 1450.8 [M+Na]$^+$ (Figure S2).

2.1.4. Synthesis of AD-1 under microwave irradiation

AD-1
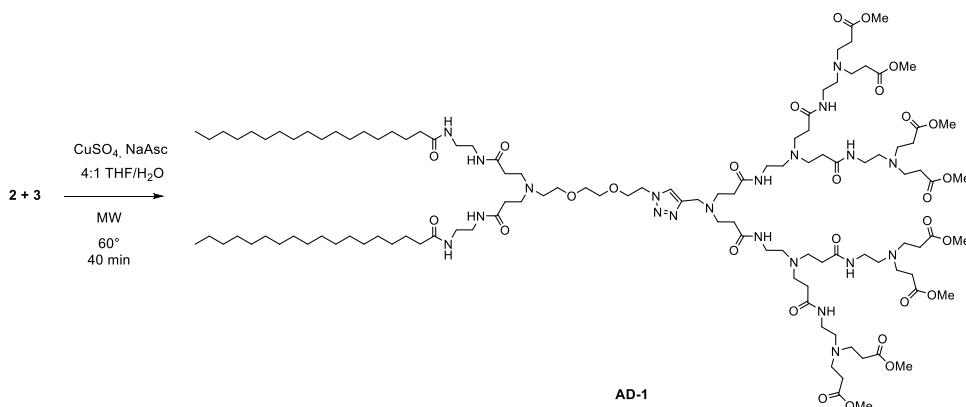
A 20 mL MW vessel was charged with 10 mL of a 4:1 THF/H$_2$O solution of azide 2 (0.51 g, 0.55 mmol) and alkyne 3 (0.71 g, 0.50 mmol), then CuSO$_4$·5H$_2$O (15 mg, 0.06 mmol) and sodium ascorbate (25 mg,

After drying over Na$_2$SO$_4$ and evaporation of the solvent the crude AD-1 was isolated in a 81% yield (1.21 g) and directly used in the next step. ^{1}H NMR (500 MHz, CDCl$_3$) δ 7.85 (bt, 2H, 2 x NHCO), 7.74 (bt, 2H, 2 x NHCO), 7.70 (s, 1H, CH=C), 7.04 (bt, 4H, 4 x NHCO), 6.99 (br, 2H, 2 x NHCO), 4.50 (t, J = 4.9 Hz, 2H, CH$_2$N-triazol), 3.85 (t, J = 4.9 Hz, 2H, OCH$_2$CH$_2$N-triazol), 3.81 (s, 2H, CH$_2$C=C), 3.67 (s, 24H, 8 x OCH$_3$), 3.56 - 3.48 (2 m, 4H, 2 x CH$_2$O), 3.44 (m, 2H, CH$_2$O), 3.34 – 3.22 (m, 20H, 10 x CH$_2$NHCO), 2.81 (m, 8H, 4 x CH$_2$N), 2.74 (t, 24H, 12 x CH$_2$N), 2.60 – 2.51 (m and t, 14H, 7 x CH$_2$N), 2.45 - 2.29 (t and m, 32H, 16 x CH$_2$CO), 2.14 (t, 4H, 2 x (CH$_2$)$_{16}$CH$_2$CO), 1.62 (m, 4H, 2 x (CH$_2$)$_{15}$CH$_2$CH$_2$CO), 1.23 (bs, 56H, 28 x CH$_2$), 0.85 (t, 6H, 2 x CH$_3$CH$_2$) ppm; ^{13}C NMR (125 MHz, CDCl$_3$): δ 174.2, 173.4, 173.0, 172.3, 172.2, 143.7, 123.9, 73.4, 70.5, 70.2, 69.4, 68.9, 52.9, 51.6, 50.1, 49.8, 49.2, 47.6, 40.1, 39.1, 37.2, 36.7, 34.0, 33.8, 33.6, 32.7, 31.9, 29.7 - 29.3, 25.8, 22.6, 14.1 ppm. ESI-TOF: 2364.6185 [$M + H$]$^+$; 1182.8182 [$M +$ 2H]$^{2+}$; 788.8820 [$M + 3$H]$^{3+}$ (Figure S3).

2.1.5. Synthesis of AD

AD

0.125 mmol) were added in sequence. The reaction was run in a microwave (MW) reactor at 60 °C for 40 min, after which the initial turbid suspension had turned to a clear, intense orange solution. TLC analysis (AcOEt/MeOH 1:1) revealed complete conversion of the reactants into a single product. THF was evaporated *in vacuo*, the residue dissolved in CH$_2$Cl$_2$ and the organic phase extracted 3 times with an EDTA solution.

Conversion of AD-1 to AD was run as described in our previous paper (Liu et al., 2014) by treating AD-1 (0.56 g, 0.24 mmol) with ethylenediamine (2 mL, 30 mmol) in a 1:1 CH$_2$Cl$_2$:MeOH (10 mL) solution under stirring at rt for 72 h. Excess ethylenediamine was removed using repeated evaporation of an azeotropic mixture of toluene and methanol (9:1). Product AD was precipitated from a 1:1 CH$_2$Cl$_2$/MeOH by

addition of Et_2O, collected after centrifugation (5500 rpm, 15 min) and discard of the supernatant liquid. The solid was dissolved in the minimum amount of water and dialyzed for 3 days, replacing water after 2 hrs, then twice a day. Lyophilization of the tube content afforded pure AD as a white solid (0.48 g, 80% yield). ^{1}H NMR (500 MHz, CD_3OD): δ 7.97 (s, 1H, CH=), 4.58 (t, C$\underline{H}_2$N-triazol), 3.90 (t, 2H, OC$\underline{H}_2$CH$_2$N--triazol), 3.82 (s, 2H, CH$_2$C≡C), 3.60 – 3.57 (2 m, 4H, 2 x CH$_2$O), 3.53 (t, 2H, CH$_2$O), 3.38 (t, 16H, 8 x C$\underline{H}_2$NHCO), 3.26 (t, 20H, 10 x C$\underline{H}_2$NHCO), 2.93 (bt, 16H, 8x CH$_2$N), 2.80 (34H, 17x CH$_2$N), 2.66 - 2.54 (12H, 6 x CH$_2$N), 2.47 – 2.31 (32H, 16 x CH$_2$CONH), 2.18 (t, 4H, 2 x -(CH$_2$)$_{16}$C$\underline{H}_2$CO), 1.60 (4H, 2 x CH$_2$CO), 1.28 (56H, 28 x CH$_2$), 0.89 (t, 6H, 2 x C$\underline{H}_3$CH$_2$) ppm; ^{13}C NMR (125 MHz, $CD_3OD/CDCl_3$ = 3:2): δ 175.2, 174.3, 173.8, 173.4, 143.1, 124.6, 70.2, 70.0, 69.1, 68.7, 52.5, 52.1, 52.0, 50.0, 49.7, 49.0, 40.0, 38.8, 38.7, 38.6, 37.2, 36.1, 33.4, 33.2, 32.3, 31.7, 29.5, 29.4, 29.2, 29.1, 25.7, 22.4, 13.5 ppm. ESI-TOF: 863.6527 $[M + 3H]^{3+}$; 647.9899 $[M + 4H]^{4+}$; 518.5918 $[M + 5H]^{5+}$; 432.6239 $[M + 6H]^{6+}$ (Figure S4).

2.2. Preparation of drug-loaded AD nanomicelles

The drug-loaded nanomicelles (DLNMs) were prepared according to the film dispersion method (Dagrada et al., 2018; Liu et al., 2021; Wei et al., 2013). Briefly, each drug were first dissolved in 1 mL of a chloroform:methanol mixture (CMM, 3:2 vol/vol) at room temperature and then mixed with 3 mg of AD dissolved in 3 mL of CMM at three different AD:drug ratios (10:1, 10:2 and 10:5 by weight). Upon solvent removal *via* rotary vacuum evaporation, the corresponding drug-containing dry lipid films were obtained. Each dry film was hydrated with phosphate-buffered saline (PBS, pH = 7.4) for 30 min at 60 °C under stirring. The nonencapsulated drug was separated first by filtration using a 0.45 μm polycarbonate membrane (Millipore Co., Bedford, MA) and then by extensive dialysis (9 h, hourly water replacement) across a membrane with a 2000 Da molecular weight cut-off. Finally, the content of the dialysis tube was lyophilized.

2.3. Dynamic light scattering

All nanomicelle size and zeta (ζ)-potential measurements were performed via dynamic light scattering (DLS) on a Zetasizer Nano-ZS (Malvern, U.K.) at 25 °C. Empty and drug-loaded AD NMs were dissolved in Milli-Q water, and were further employed for analysis at 5 mV He-Ne laser (operating wavelength λ = 633 nm, scattering angle θ = 173º). For all of the samples investigated, data showed a unimodal distribution and represent the average of at least three different measurements carried out for each sample.

2.4. Transmission electron microscopy

The morphology of AD empty and DLNMs was investigated by transmission electron microscopy (TEM). In brief, a volume of 5 mL for each NM solution was deposited on a carbon grid and then dried for 1 h. Next, the grid was stained with uranyl acetate and imaged with a Philips EM 208 (Philips, Eindhoven, the Netherland) operating at 100 kV, equipped with a Quemesa camera (Olympus Soft Imaging Solutions, Hamburg, Germany) and the RADIUS software for image acquisition.

2.5. Isothermal titration calorimetry

Isothermal titration calorimetry (ITC) experiments were performed with a MicroCal PEAQ-ITC calorimeter (Malvern, UK) at 25 °C. The cell volume was 208 μL. The micellization experiments were conducted by step-by-step injections of a constant volume of concentrated AD solution into the calorimetric cell containing Milli-Q water. Specifically, for CMC determination, a constant 1.5 μL portion of the amphiphilic dendrimer solution, at a concentration of 200 μM, was injected 24 times into the reaction cell at 150 s intervals. On the other hand, the interaction

experiments between AD micelles and DAB or VEM were carried out in PBS at pH 5 and pH 7.4, respectively. In this case, 18 injections were applied. The AD concentration in the calorimetric cell was 50 μM, while the DAB or VEM concentration in the syringe was equal to 2 mM. All solutions and buffer were degassed for 30 min at room temperature under stirring at 600 rpm prior to each experiment. After careful washing, the cell was pre-rinsed with a portion of the Milli-Q water and upon filling cell and syringe, stirring was turned and each system was allowed to thermally equilibrate for 30 min. For the micellization experiment, integrated ITC data were fitted to a sigmoidal function to yield the free enthalpy of micellization ΔH_{mic} as the difference between the final and the initial values of the integrated heat of the titration curve. The AD NM aggregation number N_{agg} was estimated from the same data set using a protocol (Laurini et al., 2021b) based on the two-state reaction model and the principle of mass conservation (see Supporting Information). Finally, the two remaining thermodynamic quantities – the free energy of micellization ΔG_{mic} (= $\Delta H_{mic} - T\Delta S_{mic}$) and the entropy variation upon micellization $T\Delta S_{mic}$ – were calculated using the values of ΔH_{mic}, N_{agg} and the degree of counterion condensation parameter β according to the procedure reported in full in Supporting Information. All experiments were run in triplicates.

2.6. Small angle X-ray scattering

Small angle X-ray scattering (SAXS) experiments were performed at the Austrian SAXS beamline of the Elettra synchrotron radiation facility (Trieste, Italy). A monochromatic radiation with a wavelength of 0.154 nm was used, and SAXS images were recorded with a 2D pixel detector Pilatus3 1 M spanning the q-range between 0.05 and 5 nm^{-1} with a resolution of 5×10^{-3} nm^{-1} (full width at half-maximum, fwhm). Calibration of detectors was performed with silver behenate powder (d-spacing = 5.838 nm). FIT2D (Hammersley, 2016) and ATSAS 3.0.5 (Manalastas-Cantos et al., 2021) were used for image conversion to one-dimensional (1D) SAXS pattern and data analysis. The scattering intensity was measured as a function of the scattering vector $q = 4\pi$ (sinθ)/λ with 2θ and λ being the scattering angle and wavelength, respectively. Experimental intensities were corrected for fluctuation of the primary intensity, transmission, and background. Scattering experiments were carried out at C = 10 μM for all samples, which were held in a 1 mm glass capillary (Hilgenberg, Malsfeld, Germany). Exposure times were 10 s, and no evidence of radiation damage was observed in the SAXS patterns. For all systems, the values of the model-independent radius of gyration R_g were obtained from a linear fitting of lnI(q) *vs.* q^2 (Guinier plot) in the low-resolution regime (*i.e.*, q < 1.3/Rg). All full scattering profiles were next fitted to a core-shell triaxial ellipsoid model with a hydrophobic core of semiaxes $a \geq b \geq c$, and a hydrophilic shell of thickness t; accordingly, the ellipsoid has a total volume $V_{tot} = 4/3\pi$ $(a + t)(b + t)(c + t)$, a core volume $V_{core} = 4/3\pi abc$, and a total model-dependent radius of gyration $R_{g,ell} = [[(a + t)^2 + (b + t)^2 + (c + t)^2)/5]]^{1/2}$. The triaxial ellipsoidal core-shell form factor plugin implemented in SASFIT (Breßler et al., 2015) with the *pcubature* routine for multi-dimensional integration was employed for data fitting. Finally, the NM aggregation number N_{agg} was determined by dividing the total volume of the dry hydrophobic core by the total alkyl chain volume. All SAXS equations, model details and explanations are given in the Supporting Information.

2.7. Nuclear magnetic resonance

NMR samples were prepared in D_2O (99.98% D) provided by Eur-Isotop (Saint Aubin, France). NMR experiments were recorded at 300 K on Bruker AVANCE spectrometer (Karlsruhe, Germany), operating at an [1]H Larmor frequency of 500 MHz, equipped with a double resonance broadband fluorine observe (BBFO) of 5 mm probe head, and z-gradient coil. Main acquisition parameters have been optimized prior to analysis: relaxation delay (D1) 5 s, 90° excitation pulse of 12.9 μs, 16 scans.
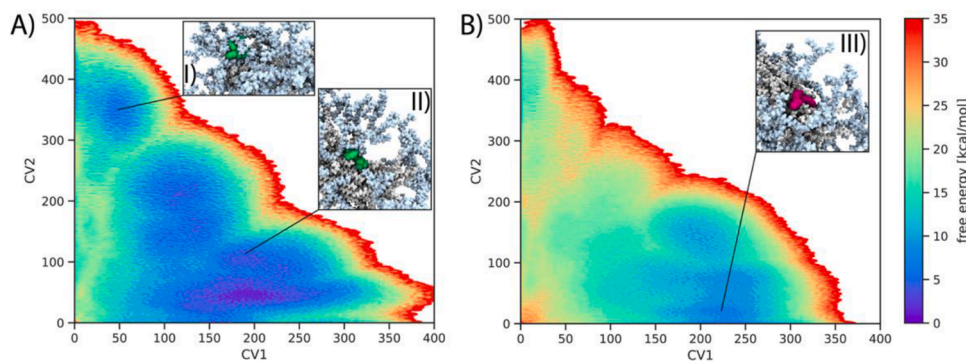
Fig. 4. Free energy surface (FES) as a function of the number of contacts between DAB (A) and VEM (B) and the hydrophobic core of the micelle (CV1, horizontal axis) or the polar shell of the AD NMs (CV2, vertical axis). Relevant conformations extracted from the MD simulations and corresponding to the free energy basins are depicted in the inserts, where the AD NM hydrophobic core atoms are represented as white spheres, the hydrophilic shell is depicted as light blue spheres and DAB and VEM molecules are shown as green and magenta spheres, respectively. (For interpretation of the references to colour in this figure legend, the reader is referred to the web version of this article.).

Diffusion parameters (^{1}H-DOSY) have been optimized for 200 ms (big delta) and 2.3 ms (little delta). 2D NMR NOESY experiments have been conducted using 32 scans, 512 complex points and 200 ms mixing time (Williams, 2005). The average molecular weight of empty and drug-loaded AD NMs was evaluated using the calibration method detailed in our previous work (Liu et al., 2011).

2.8. Drug encapsulation efficiency and drug loading capacity

For each DLNM preparation, the amount of encapsulated drug was assessed *via* absorbance measurements using the ultraviolet-visible (UV–VIS) spectrophotometer DS11-FX (DeNovix Inc., Wilmington, DE, USA) at the wavelength λ of 340 nm for DAB and 310 nm for VEM, respectively. The corresponding concentrations were then derived by interpolation using standard absorbance curves for the two anticancer drugs obtained for range of different, known drug concentrations. Drug encapsulation efficiency (EE,%) and drug loading capacity (DL,%) were then calculated according to the standard formulae, as follows:

$$EE = \frac{\text{encapsulated mass of drug}}{\text{initial mass of drug used during encapsulation}} \times 100 \qquad (1)$$

$$DL = \frac{\text{encapsualted mass of drug}}{\text{total mass of NMs}} \times 100 \qquad (2)$$

2.9. Drug release experiments

In vitro drug release profiles of DAB and VEM from the corresponding DLNMs at 37 °C were obtained using the dialysis membrane method (Kim et al., 2021). Accordingly, DAB/AD or VEM/AD NMs (1.0 mg/mL) were dispersed in 10 mM PBS at two different pH values (7.4 and 5.0, respectively) and then transferred into dialysis membranes with a molecular weight cut-off of 3000 Da (Sigma Aldrich, St. Louis, Missouri, USA). The dialysis tubes were next immersed into 15.0 mL of PBS solutions at the corresponding pH and left under stirring for a total time of 24 h. An aliquot of 1.0 mL was taken from the external dialysis solution and replaced with the same amount of fresh buffer at regular, 1 h

intervals up to 12 h, and a final withdraw was performed after 24 h. The anticancer drug concentration in the release medium was determined *via* UV–VIS spectroscopy as detailed in Section 2.8. The release profiles were fitted to the Peppas-Sahlin model (Peppas and Sahlin, 1989), a kinetic formula that specifies the diffusion and relaxation contribution to the drug dissolution process as:

$$\frac{C_t}{C_0} = k_1 t^m + k_2 t^{2m} \qquad (3)$$

in which C_t is the concentration of the drug released at time t, C_0 is the initial drug concentration, k_1 and k_2 are the velocity constants for Fickian diffusional contribution and case II relaxation contribution, respectively, and m is the Fickian diffusional release exponent (for which $m = 0.43$ for Fickian diffusion from spherical shaped objects, $m = 0.85$ for case II relaxation transport mechanisms, and $0.43 < m < 085$ in the case of anomalous transport mechanisms).

2.10. Molecular simulations

The molecular models and relevant parameterization of the AD amphiphile, DAB and VEM was taken from our previous work (Dong et al., 2018a; Russi et al., 2022). Briefly, the molecular partial charges were computed following the RESP procedure provided by the RED server (Vanquelef et al., 2011) while the antechamber program implemented in the AMBER20 suite (D.A. Case et al., 2020) was used to assign the gaff2 force-field atom types (Junmei et al., 2004) to all molecules. To characterize the interaction between DAB and VEM with AD nanomicelles we performed multiple-walker well-tempered metadynamics (wt-MetaD) simulations (Barducci et al., 2008; Raiteri et al., 2006) The use of multiple walkers allowed for trivial parallelization of the stimulations, thereby speeding up the exploration of the possible configuration of the systems under investigation. Two collective variables (CVs) were selected for the wt-MetaD simulations, namely the number of contacts made by the heavy atoms of each drug and the heavy atoms of the hydrophobic core (CV1) and the hydrophilic outer shell (CV2) of the AD molecules in the NMs, respectively. More details on the wt-MetaD
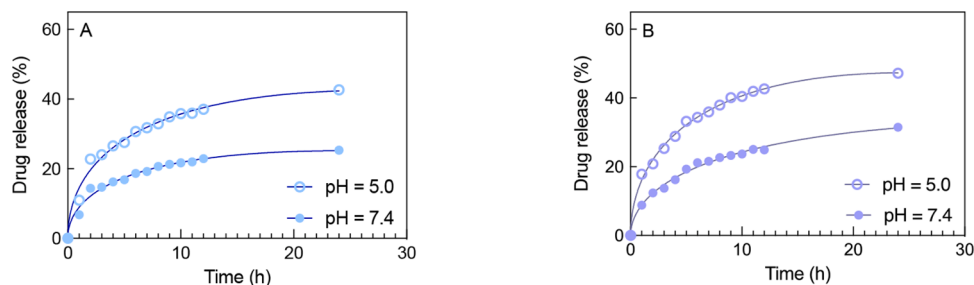

Fig. 5. Release profiles of DAB (A) and VEM (B) from AD NMs at pH = 7.4 (filled circles) and 5.0 (open circles) at 37 °C. Symbols: experimental data; continuous lines: data fitting with the Peppas-Sahlin model (Eq. (3)).
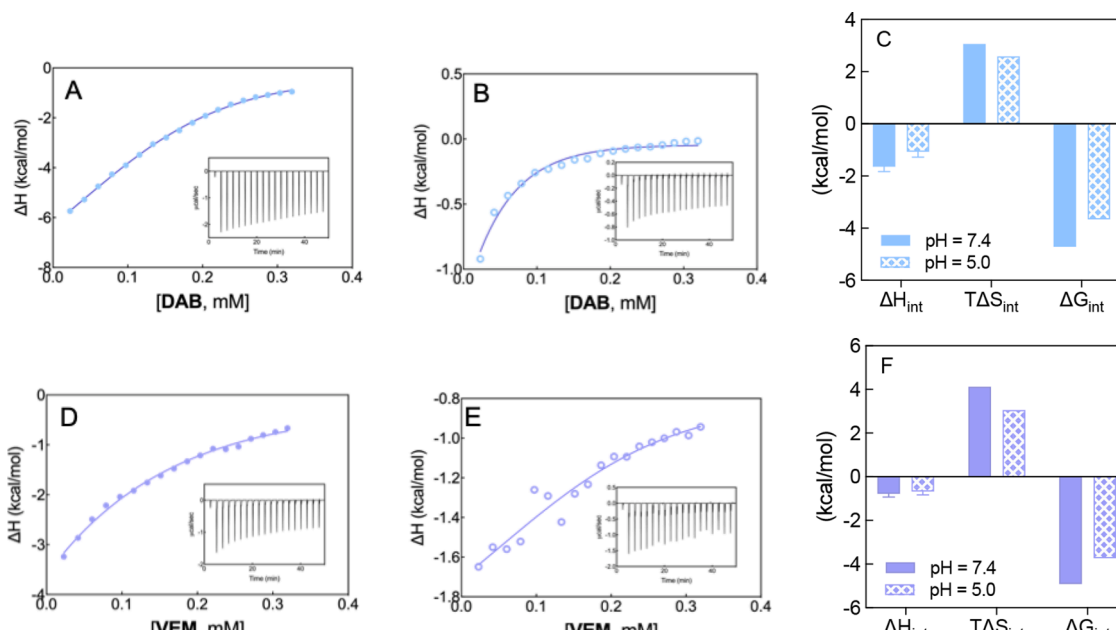
Fig. 6. Integrated ITC profiles for the interaction the AD NMs with DAB (A, pH 7.4; B, pH 5.0) and VEM (D, pH 7.4; E, pH 5.0). All measurements were performed in triplicate in PBS buffer at 37 °C. Inserts show the corresponding ITC raw data. Thermodynamic signature of the interaction of DAB (C) and VEM (F) with the AD NMs at the two pH values considered (for numerical values see Table S4).

technique and on the simulation protocols and wt-MetaD parameters are given in the Supporting Information.

2.11. Cell culture

Human malignant melanoma A-375 (CRL-1619), G-361 (CRL-1424),

SK-MEL-1 (HTB-67), CHL-1 (CRL-9446) and human embryonic kidney 293 (HEK293, CRL-1573) cells were purchased from the American Type Culture Collection (ATCC, LGC Standards SARL). Cell culture medium Dulbecco's Modified Eagle's Medium (DMEM) and Minimum Essential Medium Eagle (MEM) were purchased from Sigma-Aldrich while Mc-Coy's 5A Medium (McCoy) was purchased from ATCC. A375 and CHL-1
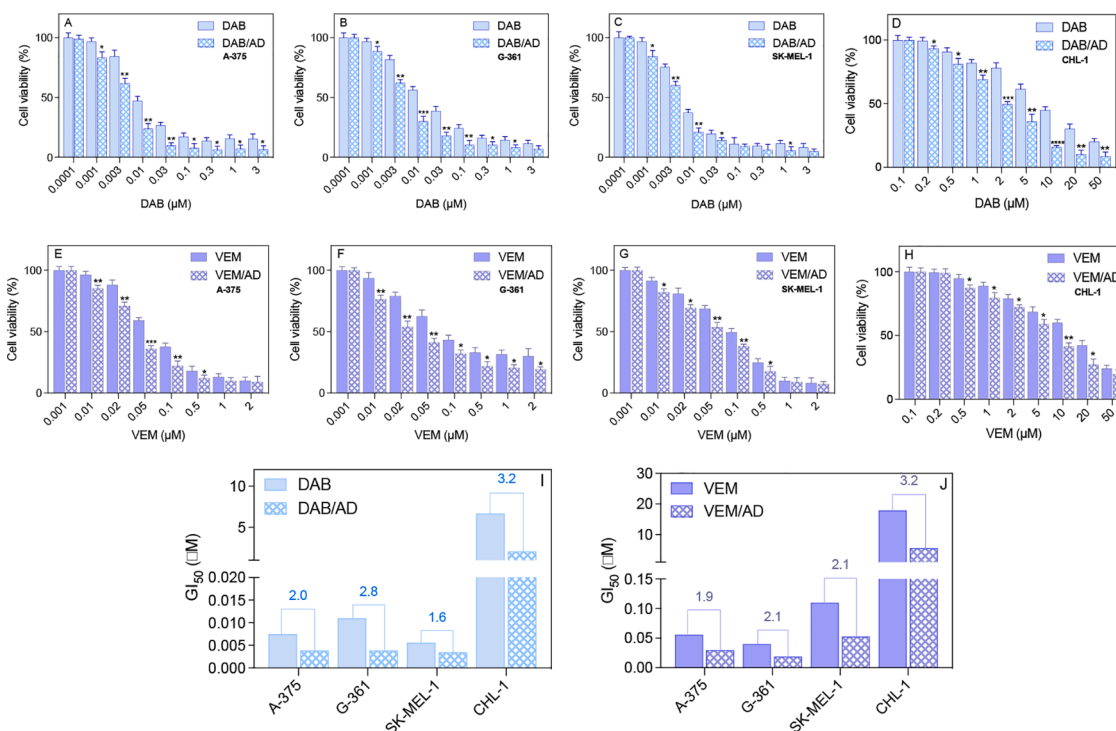

Fig. 7. Comparison of the dose-response profiles for DAB and DAB/AD NMs (top panel) and VEM and VEM/AD NMs (middle panel) in 4 different melanoma cell lines: A-375 (A,E), G-361 (B,F), SK-MEL-1 (C,G), and CHL-1 (D,H). Data are presented as mean ± SD. *, $p < 0.05$, **, $p < 0.01$ ***, $p < 0.001$, *versus* non-encapsulated drug data, as calculated by Student's t-test. The different drugs concentration used in the assays are related to the specific sensitivity of the tested cell lines to the inhibitors. (Bottom panel) Comparison of GI_{50} values (with relevant GI_{50} fold change) for DAB and DAB/AD NMs (I) and VEM and VEM/AD NMs (J) on the 4 different melanoma cell lines.

cells were maintained in DMEM containing 10% Fetal Bovine Serum (FBS, Gibco, Waltham, MA USA) and penicillin-streptomycin (pen-strep, Gibco). G-361 cells were cultured in McCoy containing 10% FBS and pen-strep. SK-MEL-1 and HEK293 cells were cultured in MEM containing 10% FBS, pen-strep, MEM Non-Essential Amino Acids Solution (Gibco) and sodium pyruvate (Gibco). All cells were cultured at 37 °C in humidified atmosphere containing 5% CO_2.

2.12. In vitro antiproliferation activity assay

To investigate the effect of DAB and VEM *per se* or encapsulated in AD NMs on cell proliferation the MTT (2,5-diphenyl-2H-tetrazolium bromide) cytotoxicity assay was performed. The different cell lines were seeded in a 96-well plate 16 h before treatment in order to permit the attachment of the cells to the plate. Next, the cells were treated either with the drug alone or with the corresponding encapsulated formulation and each 96-well plate was then cultured at 37 °C in a 5% CO_2 cell-culture incubator for 24 h. Finally, the plates were incubated with MTT at 37 °C and 5% CO_2 for 3 h. During this incubation time MTT tetrazolium salt converts into an insoluble purple MTT formazan crystals that finally gets solubilized with solubilization buffer. The absorbance was measured using the Spark® multimode microplate reader at a wavelength of 570 nm. Data are presented as a percentage relative to the non-treated control cells, using corrected absorbance (where the background signal was subtracted). All data are presented as mean ± Standard Deviation (SD) and statistical analysis was performed by Student's test (*t*-test) (GraphPad 8.0). $p \leq 0.05$ was considered significant (*); $p \leq 0.01$ (**); $p \leq 0.001$ (***). The same procedure has been applied to evaluate the toxicity of the empty AD NMs at two different concentrations (20 and 60 μM) on the same 4 melanoma cell lines and on the HEK293 cell line as representative non-cancer cellular model.

2.13. Western blot

Cells were seeded in 60 mm Petri culture dishes and allowed to grow for 24 h. Then, culture medium was replaced with fresh full medium and DLNMs at 0.2 μM. After 24 h of incubation, cells were placed on ice, washed with PBS and harvested in lysis buffer (50 mM TRIS-HCl pH 7.4, 5% SDS, 8.6% saccharide, 0.45% urea, 1 mM dithiothreitol), followed by centrifugation for 10 min at 12,000 rpm and 4 °C. Supernatants were transferred to fresh tubes, and protein content was evaluated by BCA protein assay reagent (Pierce, Rockford, IL, USA). Samples containing 25 μg of protein were separated by 12% (w/v) SDS-polyacrilamide matrix gel and transferred in a 0.22 μM nitrocellulose membrane (Schleicher & Schuell, Keene, NH, USA). The quality of transfer was determined with Ponceau S staining. Then, membranes were blocked with 5% non-fat milk in PBST for 1 h at room temperature and probed overnight at 4 °C with primary antibodies directed against the following: BRAF^{V600E} (Sigma-Aldrich, Saint-Louis, MO, USA, SAB5600047), MEK (Cell Signaling Technology Inc., Danvers, MA, USA, 9126), pMEK (Cell Signaling Technology Inc., Danvers, MA, USA, 9154), ERK1/2 (Cell Signaling Technology Inc., Danvers, MA, USA, 9102), pERK1/2 (ThermoFisher, 36–8800) and β-actin (Cell Signaling Technology Inc., Danvers, MA, USA, 4970), followed by a 1 h incubation with secondary antibodies conjugated with horseradish peroxidase directed against primary rabbit antibodies (Dako, Glostrup, Denmark, P044801–2). BRAF^{V600E} and MEK were used at 1:500 dilution. ERK1/2, pMEK and pERK1/2 were used at 1:250 dilution while β-actin at final 1:10,000 dilution. Finally, membranes were incubated with ECL substrate (Bio-Rad, Hercules, CA, USA), and the chemiluminescent signal was acquired with ChemiDoc (Bio-Rad, Hercules, CA, USA) using ImageLab software (ver. 6.0, Bio-Rad, Hercules, CA, USA).

2.14. Caspase 3/7 activation

Caspase 3/7 activation in the melanoma A-375 cell line was detected using the Caspase-Glo® 3/7 Assay (Promega Madison, WI, USA) following the manufacturer's protocol. Briefly, 100 μL of a 100,000 cells/mL solution was pipetted in white 96-well plates and incubated for 24 h to allow the cells to adhere. Afterwards, freshly prepared DAB/AD and VEM/AD solutions were added to the cells, and the cells were treated for 24 h. Staurosporine (Abcam, Cambridge, UK) served as the positive control. For analysis, a Caspase-Glo® 3/7 reagent was prepared and added to the cells. Finally, luminescence was measured using the GloMax® 20/20 (Promega Madison, WI, USA). All assays were performed in triplicate.

3. Results and discussion

3.1. Synthesis of the amphiphilic dendrimer AD

The amphiphilic dendrimer AD was synthetized by optimizing some of the steps of the synthetic route reported in our previous work (Liu et al., 2014). The central step of the synthesis is a Copper-Catalyzed Azide-Alkyne Cycloaddition (CuAAC) between the lipophilic azide 2 and the alkyne partner 3, leading to the dendrimeric octaester AD-1, that in turn is converted into the final amphiphilic AD by aminolysis with ethylenediamine. The key modification performed in this work involves the crucial click chemistry reaction step, that here was run under MW irradiation. After an extensive optimization procedure involving screening of solvent, reaction times, temperature and reactant ratio, we found that complete conversion into the product was afforded by running the MW mediated reaction at 60° in 40 min, in a 4:1 THF/H_2O solution, with 10% Cu(II) and 25% ascorbate. Moreover, the lipophilic azide 2 was also prepared by a simplified method, involving the coupling of the diamine 1 with the highly reactive stearoyl chloride in CH_2Cl_2. The original protocol (Liu et al., 2014), based on the condensation between stearic acid and the diamine 1 mediated by N,N'-dicarbonyldiimidazole in DMF, led in our hands to mixtures of mono- and diamide products requiring complex and lengthy separation procedure. Overall, our optimized conditions resulted in improved yields, simplified workup methodologies and shortening of overall process time.

3.2. Characterization of empty and drug-loaded AD nanomicelles

3.2.1. Transmission electron microscopy and dynamic light scattering analysis

The transmission electron microscopy (TEM) analysis of the dried empty and drug-loaded AD systems revealed in all cases the formation of nanomicelles with a diameter of the order of 10 nm and with a round morphology (Fig. 2A-C). The values of the hydrodynamic diameter R_h (and the ζ-potential) of the same systems, measured in aqueous solution, were found to be 10.2 ± 0.2 nm (ζ = +27 mV) for the empty AD (Fig. 2D) NMs and 9.9 ± 0.4 nm (ζ = +25 mV) and R_h = 9.6 ± 0.3 (ζ = +25 mV) for DAB- and VEM-loaded NMs (Fig. 2E and F), respectively, yielding a first indication that the encapsulation of each anticancer cargo did not modify substantially the size, the shape and the electrokinetic potential of the nanocarrier (see below for further data and discussion). Of note, AD solutions were found to be stable upon storage at 4 °C for 3 months in the dark, as confirmed by DLS (data not shown).

3.2.3. Self-assembling thermodynamics of empty AD nanomicelles by isothermal titration calorimetry

The self-assembly of AD into NMs was next characterized using a validated protocol based on isothermal titration calorimetry (ITC) (Laurini et al., 2021b). ITC experiments (Fig. 2G) yielded a critical micellar concentration (CMC) for AD of 5.4 μM, in excellent agreement with the value of 3.2 μM previously obtained for the same system by a fluorescence spectroscopic-based assay (Wei et al., 2015), and in line with CMC values obtained for similar dendron-based amphiphiles (Dhumal et al., 2021). From the thermodynamics viewpoint, during the demicellization process the injection of a concentrated AD solution into

water mostly resulted in exothermic signals (Fig. 2G, insert); accordingly, for the reverse process of AD micellization, a correspondingly positive (endothermic) micellization enthalpy value of $\Delta H_{mic} = +5.06 \pm 0.12$ kcal/mol could be obtained from the integrated demicellization data fitting as the difference between the final and the initial heat in the titration curve. The adopted ITC protocol (see Supporting Information) further allowed to determine the two remaining quantities required to fully describe the thermodynamics of the micellization process, *i.e.*, the Gibbs free energy of micellization (ΔG_{mic}) and its entropic component ($T\Delta S_{mic}$), along with the aggregation number (N_{agg}) of the AD NMs. Specifically, the derived values of the two thermodynamic quantities were $\Delta G_{mic} = -11.11$ kcal/mol and $T\Delta S_{mic} = +16.17$ kcal/mol, respectively. As indicated by the negative sign of ΔG_{mic}, AD self-assembly in water is a thermodynamically spontaneous process, principally driven by the formation of a strong network of hydrophobic interactions among the double-alkylic portion of the amphiphiles and the subsequent release of AD and drug-bound water molecules into the bulk solvent upon drug encapsulation ($T\Delta S_{mic} > 0$). At the same time, the positive enthalpic component reports the overall balance between (favorable) hydrogen bonding and polar interactions among the dendron branches and the (unfavorable) electrostatic repulsions of the positively charged terminal groups. Finally, the ITC estimated value for N_{agg} was 18 ± 1, in agreement with the values derived from SAXS and NMR experiments, as further discussed in §3.2.4 and §3.2.6, respectively.

3.2.4. Small angle X-ray scattering

Small angle X-ray scattering (SAXS) findings were then performed to verify DLS and TEM data about the size and shape of empty and drug-loaded AD NMs, and to acquire further information regarding their internal structure. The scattering intensity I(q) as a function of the momentum transfer q for the self-assembled AD system at 10 µM (> CMC) is shown in Fig. 2H. The good linearity of data in the Guinier region indicates that the micelle distribution is approximately monodisperse, in agreement with DLS and TEM evidences (Fig. 2A and D). Accordingly, the corresponding value of R_g could be estimated from the Guinier approximation (Eq. (S7) and insert in Fig. 2H), and found to be equal to 3.39 ± 0.01 nm. Under the condition of negligible interparticle correlation, the solution structure factor S(q,c) in Eq. (S6) is equal to 1, and a model for the particle form factor P(q) can be used to describe the scattering data. Specifically, the scattering profile of AD micelles could be well modeled by a two-component ellipsoid form factor, as shown by the red curve in Fig. 2H. According to the model, AD micelles can be described as a triaxial ellipsoid (Figure S5, left and Eq. (S8)), with semiaxes $a = 2.60$ nm, $b = 2.11$ nm, and $c = 1.84$ nm for the hydrophobic core, while a value of 2.10 nm was found for the shell thickness parameter t, leading to the final ellipsoid dimensions $(a + t) = 4.70$ nm, $(b + t) = 4.21$ nm, and $(c + t) = 3.94$ nm, respectively. Finally, a model-dependent value of the radius of gyration $R_{g,ell}$ of 3.33 nm was calculated, in agreement with model-independent counterpart discussed above (3.39 nm). Analogous SAXS profiles were obtained in the presence of either anticancer drug (Figure S5, right), implying that encapsulation of DAB or VEM did not substantially change the core/entire size and shape of the corresponding DLNMs (see Table S1 for a comparison), in agreement with the evidences provided by TEM and DLS (§3.2.1). Finally, the value of the aggregation number for empty and drug-loaded AD NMs computed from the core-shell triaxial ellipsoid model via Eq. (S14) ($N_{agg} = 17$, Table S1) are in line with those obtained from both the ITC data presented above (§3.2.3) and NMR experiments (§3.2.6), as discussed below.

3.2.5. Drug encapsulation efficiency and drug loading capacity of the AD nanomicelles

Panel I in Fig. 2 shows the trend in encapsulation efficiency (EE) and drug loading capacity (DL) for the DAB- and VEM-loaded AD NMs at three different values of the AD/drug weight ratio (AD/D) (see Table S2

for the full set of numerical values). For both nanosystems, EE only slightly decreases while, concomitantly, the DL progressively increases. Interestingly, at the highest AD/D considered (10:5), the DL of the NMs reached the values of $26.8 \pm 1.3\%$ (AD/DAB) and $24.2 \pm 2.9\%$ (AD/VEM), and the encapsulation efficiency was approximately $68.8 \pm 3.0\%$ and $57.7 \pm 5.1\%$ for DAB and VEM, respectively. These results indicate that both nanosystems have very good EE and DL capacity, in line with previous evidences obtained for AD NMs using doxorubicin as the encapsulated drug (Wei et al., 2015).

3.2.6. Nuclear magnetic resonance

NMR diffusion experiments (DOSY) have been carried on the aqueous solution of AD, DAB/AD (1:5 molar ratio) and VEM/AD (1:5 molar ratio) NMs (Fig. 3). For the empty AD NMs, ^{1}H-DOSY showed the formation of homogeneous micellar species, for which the self-diffusion coefficient (D_{self}) was calculated to be equal to 3.97×10^{-11} m^2/s; (Fig. 3A) in addition, from the corresponding NMR-derived molecular weight an average aggregation number (N_{agg}) of 16 amphiphile molecules was calculated for the AD NMs, in line with ITC (§3.2.3) and SAXS (§3.2.4) data. DOSY spectra recorded on drug-loaded AD NMs showed homogeneous diffusion of both systems, which confirmed the concomitant self-diffusion of the involved species (AD and drug, respectively) (Fig. 3B,C).

Importantly, the calculated D_{self} values were similar ($D_{self} = 4.72 \times 10^{-11}$ m^2/s and 4.09×10^{-11} m^2/s DAB- and VEM- loaded AD NMs, respectively), and very close to the value derived for the cargo-free AD NMs, suggesting no alteration in the micellar aggregation number upon drug loading. To further investigate the encapsulation process and eventually determine the location of each drug within the AD NMs, 2D-NOESY experiments were recorded on both empty and AD DLNMs. Dipolar interaction due to the proximity of hydrogen atoms through space successfully provided information about the relative position of drug compared to the self-assembled AD amphiphiles. In the case of the DAB/AD complex, the observed NOE cross peaks show a proximity between the hydrogen atoms of the drug and all of the AD protons, suggesting a more uniform distribution of the drug within the corresponding NM (Figure S6, left). Contrarily, for the VEM/AD NMs only the hydrophobic component of AD presents NOE correlations with the protons belonging to the drug, suggesting a preferential location of VEM in the proximity of the NM core (Figure S6, right).

3.2.7. Modeling of DAB e VEM interaction with the AD nanomicelles

The NMR evidences presented above suggest differential interactions of DAB and VEM with the different regions (*i.e.*, core and shell) of the AD NMs. To investigate this aspect further, we performed a set of well-tempered metadynamics simulations (wt-MetaD). The free energy surfaces (FES) along the selected collective variables (CVs) obtained for both DAB and VEM within the corresponding AD NMs are reported in Fig. 4.

As it can be seen in panel A of Fig. 4, favorable interactions of DAB with the AD NMs components (represented by dark blue regions) are detected for an extensive range of configurations. Particularly, one free energy basin is characterized by a high number of contacts between DAB and the polar heads of AD (centered at 350 contacts along CV2) and, contextually, by a substantially lower number of contacts with the hydrophobic core of the micelle along CV1. This configuration corresponds to a situation in which the drug is preferentially located within the hydrophilic outer shell of the AD NMs, and is further stabilized in that position by favorable interactions with the flexible polar terminals of the AD amphiphiles (see insert I in Fig. 4A). Another (broader) favorable free energy region is detected for the DAB/AD NM system, corresponding to a situation in which the anticancer drug establishes a great number of contacts with the hydrophobic portion of AD (from 100 to 300 contacts along CV1) and with the hydrophilic portion of the AD nanomicelle (from 0 to ~220 contacts along CV2), respectively (Fig. 4A). This second free energy basin is representative of a DAB

molecule located in the proximity of the hydrophobic core of the NM, with some of the hydrophilic AD branches slightly backfolding to allow for that further drug stabilization, as highlighted by the representative snapshot shown as insert II in Fig. 4A. In contrast, the simulated FES for the alternative VEM/AD NM system reported in panel B in Fig. 4 shows only one region of favorable conformations, characterized by a high number of contacts between the drug and the hydrophobic core of the nanomicelle (from 0 to 180 contacts between VEM and the hydrophilic shell along CV1). This corresponds to a situation in which the VEM is predominantly located in the close proximity of the hydrophobic core of AD NMs while seldom contacting just a small number of the AD hydrophilic branches, as illustrated by the representative snapshot shown as insert III in Fig. 4B. Accordingly, the different location distributions and interaction modes of DAB and VEM within the AD NMs uncovered by the wt-MetaD simulations are in excellent agreement with the results obtained by NMR experiments presented and discussed in the previous section.

3.2.8. Release kinetics from the drug-loaded nanomicelles

The *in vitro* release kinetics of nanocarriers gives information on their potential to modulate drug release, and is thus an essential parameter to be considered in the overall assessment of the safety, efficacy, and quality of the relevant nanoformulation. When appropriately conducted, these measurements can be correlated to *in vivo* behavior through predictive mathematical models (Kostewicz et al., 2014; Sjögren et al., 2014; Tsume et al., 2014), eventually leading to an acceleration of regulatory approval (Weng et al., 2020). The dialysis membrane (DM) method is likely the most popular procedure to test the *in vitro* release kinetics of nanoparticles (D'Souza, 2014; Kim et al., 2021) and, irrespective of the different set-ups, this procedure always relies on a semi-permeable membrane to achieve physical separation of the nanoparticle and the free drug. Fig. 5 shows the release profiles of DAB and VEM from the corresponding loaded AD NMs obtained at pH = 7.4 and 5.0, selected to mimic a neutral physiological condition and a tumor acidic microenvironment, respectively.

In order to better compare these data and to describe the underlying drug release mechanism from the AD nanovectors, we successfully fitted the corresponding experimental release profiles to Eq. (3) (see Table S3 for the full set of fitting parameters). For both DLNM systems at two different pH considered, the estimated release exponent m is close to the "ideal" value of 0.43 for Fickian diffusion from spherical systems (*i.e.*, 0.40 for DAB/AD at both pH values and 0.44 and 0.42 for VEM/AD at pH 7.4 and 5.0, respectively, Table S3). The evidence that all release processes followed a diffusion mechanism is additionally substantiated by the fact that the values of the kinetic constant k_1 are positive and substantially higher than those estimated for k_2. Moreover, all k_2 values have negative signs, supporting the notion that the contribution of the corresponding release component in the release process is negligible. Of note, a negative sign for k_2 might indicate inhibited release, eventually explained by a two-stage release with a strong initial burst and almost constant release after that (Huang et al., 2018); such condition, however, does not seem to apply to the present systems given the trend exhibited by the experimental release profiles (Fig. 5). Data in Fig. 5 also show that, in analogy to what we observed for similar self-assembling amphiphilic systems (Liu et al., 2021; Wei et al., 2015), both DAB/AD and VEM/AD NMs release their drug payloads more efficiently at pH 5 than at pH 7.4 – an advantageous feature for effective drug delivery at the tumor side and reduced systemic toxicity. In detail, a maximum of 25% and 43% of DAB is released from the DAB/AD NMs at pH 7.4 and 5, respectively, whilst slightly higher amounts of VEM – 31% and 47% – are recovered from the alternative nanosystem under the same conditions. With the view of finding a molecular-based rationale for the observed differential release of the two anticancer drugs from their AD nanocarriers at neutral and acidic pH, ITC experiments were further exploited to investigate the interaction of DAB and VEM with the AD NMs, as detailed below.

3.2.9. Interaction thermodynamics of DAB and VEM with the AD nanomicelles

Fig. 6 and Table S4 gathers all results obtained from ITC measurements aimed at characterizing the thermodynamics of interaction between the AD NMs and their small-molecule cargoes in buffered solution of pH = 7.4 and 5.0, respectively. Examining the thermodynamic characteristics provided in Fig. 6C,F and Table S4 indicated that drug-nanomicelle interactions in both systems are mostly entropic in nature (TΔS_{int} >0). Despite the fact that exothermic contributions are observed in all instances (ΔH_{int} <0), the driving force of DAB and VEM binding to AD NMs originates from the substantial, positive entropic changes, which ultimately determines the total negative value of interaction free energy (ΔG_{int} < 0, Fig. 6C,F and Table S4). More interestingly, however, a comparison of ITC data at pH 7.4 and 5.0 reveals that the values of ΔG_{int} (−4.91 kcal/mol and −4.71 kcal/mol for DAB/AD and VEM/AD, respectively) are substantially more favorable under neutral pH settings than those recovered in the alternative, more acidic environment (ΔG_{int} = −3.73 kcal/mol and −3.66 kcal/mol for DAB/AD and VEM/AD, respectively, Fig. 6C,F and Table S4).

These results correspond with the respective drug release characteristics at the two pH levels discussed in §3.2.8 (see Fig. 5). In fact, at pH 7.4, the strongest intermolecular interactions between DAB and VEM with the AD NMs result in a significantly slower drug release from the respective systems, whereas at a more acidic pH, the interactions between both drugs and the AD nanovectors are weaker, ultimately resulting in a faster release profile.

3.3. In vitro anticancer activity assays of drug-loaded AD nanomicelles

The cytotoxic effects of the free and AD NM-delivered anticancer drugs were finally evaluated in 4 melanoma cell lines. Among these, the A-375 cell line carries a homozygous BRAF^{V600E} mutation, the G-361 and SK-MEL-1 cell lines are heterozygous for the same amino acid variation, while the CHL-1 cell line is homozygous for wild-type BRAF. Although immune profiles of patient tumors are absent in all cell lines, a recent study has shown that the specific cell panel selected in this work recapitulate well the mutational and transcriptional profiles of the respective malignancies (Vincent and Postovit, 2017). As shown in Fig. 7A-H (and Figures S7 and S8), not only all melanoma cells have a consistent response to both DAB- and VEM-loaded AD NMs, which results in an effective concentration-dependent inhibition of cell proliferation, but also the potency of both DLNMs is 2–3 times higher than that of the free clinical drugs.

Considering the three cell lines bearing the V600E-mutated BRAF, while the GI$_{50}$ values for free DAB-based treatments varies in the range 0.0056 – 0.011 μM, with an average GI$_{50}$ of 0.0080 μM, the same quantity is below 0.0040 μM in all cases (average GI$_{50}$ = 0.0037 μM) (see Fig. 7I and S7). Similarly, in the same cell line set free VEM inhibits cell proliferation with GI$_{50}$ values from 0.040 to 0.11 μM (average GI$_{50}$ = 0.069 μM), whereas the VEM/AD NMs are substantially more effective (Fig. 7J and S8), with an average GI$_{50}$ of 0.034 μM. It is interesting to observe that an enhanced response is also reported for both the DAB/AD and VEM/AD nanosystems on the last melanoma cell line considered (CHL-1), which constitutively expresses wild-type BRAF against which both drugs are reported to be less potent, and was used as a reference system. Interestingly, the cytotoxicity of the pristine AD NMs against the four tested melanoma cell lines was particularly low even at the highest concentration tested (60 μM, Figure S9) corroborating that the antitumor activity is prevalently dependent on the drugs. Additionally, the viability of the empty AD NMs in a non-cancer (HEK293) cell line (77% at the maximum concentration tested of 160 μM, Figure S9, right) confirmed that this system itself is characterized by a limited intrinsic cytotoxicity. Finally, the inhibition of the MAPK pathway by the DAB/AD and VEM/AD NMs and the related induction of cell apoptosis were confirmed via western blot and caspase 3/7 activation assays. As shown in the left panel of Figure S10, MEK and ERK1/2 phosphorylation was

inhibited at a drug concentration of 0.2 μM using both DLNMs; concomitantly, an increase in caspase 3/7 activation was detected by treating the same cell lines with different concentrations of each of the anticancer drug encapsulated within the AD NMs (last two panels in Figure S10). In aggregate, all these results obtained with the DAB- and VEM-loaded AD NMs appear to be quite promising and demonstrate the good anticancer activity of these systems compared to the clinical free drug alone.

4 Conclusions

Melanoma is a very aggressive cancer that has historically been extremely difficult to treat. Nonetheless, following decades of fundamental study into the signal transduction pathways that increase cancer cell survival, chemoresistance, growth, and immunological interaction, targeted therapies have been created that provide better survival for patients afflicted by this malignant pathology. In this arena, selective BRAF inhibitors like dabrafenib and vemurafenib, which selectively inhibit tumor cell proliferation in patients harboring the activating BRAF^{V600E} mutation, are among the most promising therapies that have been developed. Although these therapies provide patients with optimism, they are not without downsides, including serious side effects and, almost unavoidably, eventual recurrence. Nanotherapeutics bears significant potential to bypass these limitations, and can further open new avenues in alternative, more effective yet still patient-compliant administration routes (*e.g.*, MNs) or in the delivery of several anticancer drugs simultaneously. Indeed, different drug metabolic pathways are one of the primary reasons why many combinatorial treatments have failed in clinical trials; as a result, encapsulation in a nanocarrier may avoid this hurdle by shielding the active principle from being metabolized until they reach their target. In our view, delivering BRAFis or BRAFi/MEKi formulations with the aid of a suitable nanocarrier such as the NMs formed by the amphiphilic dendrimer AD can offer a cornucopia of advantages in the future treatment of melanoma which include – but are not limited to – the possibility of i) delivering drug combinations with a single formulation, ii) exploiting the enhanced tissue permeability and improved systemic drug circulation, both of which might boost the bioavailability of anti-melanoma chemotherapeutics to metastatic tumors; iii) benefitting from the gradual release of the anticancer drugs inside the cells of the tumor, and iv) achieving the targeted reduction of systemic toxicity of chemotherapeutics, ultimately leading to a decrease in the number of unintended side effects. We are also fully aware that the road to the adoption of nanotechnology, and in particular to self-assembled nanoobjects as drug carriers, is hampered by a series of major obstacles. These comprise extensive *in vivo* preclinical studies for efficacy and, above all, toxicity and unintended immune system stimulation on the clinical side and high production costs due to the complexity of the nanomaterial composition, which might make scaling up difficult, from the engineering standpoint, just to name a few. However, the overall encouraging results we achieved with the encapsulation, release and activity of DAB and VEM into our AD NMs lead us to the conclusion these DLNMs could deserve further studies to ascertain their *in vivo* activity. Contextually, in our laboratory we are currently extending the study to the encapsulation of different BRAFi/MEKi formulations within our AD NMs, with the hope of achieving enhanced synergistic anticancer activity against melanoma cells.

Data availability

Data will be made available on request.

Acknowledgments

Supplementary materials

Supplementary material associated with this article can be found, in the online version, at doi:10.1016/j.ejps.2022.106311.

References

Arnold, M., Singh, D., Laversanne, M., Vignat, J., Vaccarella, S., Meheus, F., Cust, A.E., de Vries, E., Whiteman, D.C., Bray, F., 2022. Global burden of cutaneous melanoma in 2020 and projections to 2040. JAMA Dermatol. 158, 495–503.

Barducci, A., Bussi, G., Parrinello, M., 2008. Well-tempered metadynamics: a smoothly converging and tunable free-energy method. Phys. Rev. Lett. 100, 020603.

Bollag, G., Tsai, J., Zhang, J., Zhang, C., Ibrahim, P., Nolop, K., Hirth, P., 2012. Vemurafenib: the first drug approved for BRAF-mutant cancer. Nat. Rev. Drug Discov. 11, 873–886.

Breßler, I., Kohlbrecher, J., Thünemann, A.F., 2015. SASfit: a tool for small-angle scattering data analysis using a library of analytical expressions. J. Appl. Crystallogr. 48, 1587–1598.

Budin, G., Dimala, M.M., Lamour, V., Oudet, P., Mioskowski, C., Meunier, S., Brino, L., Wagner, A., 2010. A chemical labeling strategy for proteomics under nondenaturing conditions. ChemBioChem 11, 79–82.

Cantwell-Dorris, E.R., O'Leary, J.J., Sheils, O.M., 2011. BRAFV600E: implications for carcinogenesis and molecular therapy. Mol Cancer Ther 10, 385–394.

Carr, M.J., Sun, J., Eroglu, Z., Zager, J.S., 2020. An evaluation of encorafenib for the treatment of melanoma. Expert Opin. Pharmacother. 21, 155–161.

Chapman, P.B., Hauschild, A., Robert, C., Haanen, J.B., Ascierto, P., Larkin, J., Dummer, R., Garbe, C., Testori, A., Maio, M., Hogg, D., Lorigan, P., Lebbe, C., Jouary, T., Schadendorf, D., Ribas, A., O'Day, S.J., Sosman, J.A., Kirkwood, J.M., Eggermont, A.M., Dreno, B., Nolop, K., Li, J., Nelson, B., Hou, J., Lee, R.J., Flaherty, K.T., McArthur, G.A., 2011. Improved survival with vemurafenib in melanoma with BRAF V600E mutation. N. Engl. J. Med. 364, 2507–2516.

Chapman, P.B., Robert, C., Larkin, J., Haanen, J.B., Ribas, A., Hogg, D., Hamid, O., Ascierto, P.A., Testori, A., Lorigan, P.C., Dummer, R., Sosman, J.A., Flaherty, K.T., Chang, I., Coleman, S., Caro, I., Hauschild, A., McArthur, G.A., 2017. Vemurafenib in patients with BRAFV600 mutation-positive metastatic melanoma: final overall survival results of the randomized BRIM-3 study. Ann. Oncol. 28, 2581–2587.

Case, D.A., Aktulga, H.M., Belfon, K., et al., 2020. AMBER 2020. University of California, San Francisco (CA, USA).

D'Souza, S., 2014. A review of *in vitro* drug release test methods for nano-sized dosage forms. Adv. Pharm. 2014, 304757.

Dagrada, G., Rupel, K., Zacchigna, S., Tamborini, E., Pilotti, S., Cavalleri, A., Fechner, L. E., Laurini, E., Smith, D.K., Buxton, S., Pricl, S., 2018. Self-assembled nanomicelles as curcumin drug delivery vehicles: impact on solitary fibrous tumor cell protein expression and viability. Mol. Pharm. 15, 4689–4701.

Dankner, M., Rose, A.A.N., Rajkumar, S., Siegel, P.M., Watson, I.R., 2018. Classifying BRAF alterations in cancer: new rational therapeutic strategies for actionable mutations. Oncogene 37, 3183–3199.

Dhumal, D., Lan, W., Ding, L., Jiang, Y., Lyu, Z., Laurini, E., Marson, D., Tintaru, A., Dusetti, N., Giorgio, S., Iovanna, J.L., Pricl, S., Peng, L., 2021. An ionizable supramolecular dendrimer nanosystem for effective siRNA delivery with a favorable safety profile. Nano Res 14, 2247–2254.

Dong, Y., Yu, T., Ding, L., Laurini, E., Huang, Y., Zhang, M., Weng, Y., Lin, S., Chen, P., Marson, D., Jiang, Y., Giorgio, S., Pricl, S., Liu, X., Rocchi, P., Peng, L., 2018a. A dual targeting dendrimer-mediated siRNA delivery system for effective gene silencing in cancer therapy. J. Am. Chem. Soc. 140, 16264–16274.

Dummer, R., Ascierto, P.A., Gogas, H.J., Arance, A., Mandala, M., Liszkay, G., Garbe, C., Schadendorf, D., Krajsova, I., Gutzmer, R., Chiarion Sileni, V., Dutriaux, C., de Groot, J.W.B., Yamazaki, N., Loquai, C., Moutouh-de Parseval, L.A., Pickard, M.D., Sandor, V., Robert, C., Flaherty, K.T., 2018. Overall survival in patients with BRAF-mutant melanoma receiving encorafenib plus binimetinib *versus* vemurafenib or encorafenib (COLUMBUS): a multicentre, open-label, randomised, phase 3 trial. Lancet Oncol 19, 1315–1327.

Ellert-Miklaszewska, A., Ochocka, N., Maleszewska, M., Ding, L., Laurini, E., Jiang, Y., Roura, A.J., Giorgio, S., Gielniewski, B., Pricl, S., Peng, L., Kaminska, B., 2019. Efficient and innocuous delivery of small interfering RNA to microglia using an amphiphilic dendrimer nanovector. Nanomedicine 14, 2441–2458.

Garnett, M.J., Marais, R., 2004. Guilty as charged: B-RAF is a human oncogene. Cancer Cell 6, 313–319.

Hamid, O., Cowey, C.L., Offner, M., Faries, M., Carvajal, R.D., 2019. Efficacy, safety, and tolerability of approved combination BRAF and MEK inhibitor regimens for BRAF-mutant melanoma. Cancers (Basel) 11, 1642.

Hammersley, A.P., 2016. FIT2D: a multi-purpose data reduction, analysis and visualization program. J. Appl. Crystallogr. 49, 646–652.

Haugh, A.M., Salama, A.K.S., Johnson, D.B., 2021. Advanced melanoma: resistance mechanisms to current therapies. Hematol. Oncol. Clin. North. Am. 35, 111–128.

Hauschild, A., Grob, J.J., Demidov, L.V., Jouary, T., Gutzmer, R., Millward, M., Rutkowski, P., Blank, C.U., Miller Jr., W.H., Kaempgen, E., Martín-Algarra, S., Karaszewska, B., Mauch, C., Chiarion-Sileni, V., Martin, A.M., Swann, S., Haney, P., Mirakhur, B., Guckert, M.E., Goodman, V., Chapman, P.B., 2012. Dabrafenib in BRAF-mutated metastatic melanoma: a multicentre, open-label, phase 3 randomised controlled trial. Lancet 380, 358–365.

Holderfield, M., Deuker, M.M., McCormick, F., McMahon, M., 2014. Targeting RAF kinases for cancer therapy: bRAF-mutated melanoma and beyond. Nat. Rev. Cancer 14, 455–467.

Huang, W., Tsui, C.P., Tang, C.Y., Gu, L., 2018. Effects of compositional tailoring on drug delivery behaviours of silica xerogel/polymer core-shell composite nanoparticles. Sci. Rep. 8, 13002.

Junmei, W., Romain, M.W., James, W.C., Peter, A.K., David, A.C., 2004. Development and testing of a general amber force field. J. Comput. Chem. 25, 1157–1174.

Kim, Y., Park, E.J., Kim, T.W., Na, D.H., 2021. Recent progress in drug release testing methods of biopolymeric particulate system. Pharmaceutics 13, 1313.

Koelblinger, P., Thuerigen, O., Dummer, R., 2018. Development of encorafenib for BRAF-mutated advanced melanoma. Curr. Opin. Oncol. 30, 125–133.

Kostewicz, E.S., Abrahamsson, B., Brewster, M., Brouwers, J., Butler, J., Carlert, S., Dickinson, P.A., Dressman, J., Holm, R., Klein, S., Mann, J., McAllister, M., Minekus, M., Muenster, U., Müllertz, A., Verwei, M., Vertzoni, M., Weitschies, W., Augustijns, P., 2014. *In vitro* models for the prediction of *in vivo* performance of oral dosage forms. Eur. J. Pharm. Sci. 57, 342–366.

Laurini, E., Aulic, S., Marson, D., Fermeglia, M., Pricl, S., 2021a. Cationic dendrimers for siRNA delivery: an overview of methods for in vitro/in vivo characterization. Methods Mol. Biol. 2282, 244–266.

Laurini, E., Aulic, S., Skoko, N., Marson, D., Fermeglia, M., Pricl, S., 2021b. ITC for characterization of self-assembly process of cationic dendrons for siRNA delivery. Methods Mol. Biol. 2282, 245–266.

Lee, J.W., Kim, B.-.K., Kim, H.J., Han, S.C., Shin, W.S., Jin, S.-.H., 2006. Convergent synthesis of symmetrical and unsymmetrical PAMAM dendrimers. Macromolecules 39, 2418–2422.

Lee, K., Goudie, M.J., Tebon, P., Sun, W., Luo, Z., Lee, J., Zhang, S., Fetah, K., Kim, H.-.J., Xue, Y., Darabi, M.A., Ahadian, S., Sarikhani, E., Ryu, W., Gu, Z., Weiss, P.S., Dokmeci, M.R., Ashammakhi, N., Khademhosseini, A., 2020. Non-transdermal microneedles for advanced drug delivery. Adv. Drug Deliv. Rev. 165-166, 41–59.

Lito, P., Rosen, N., Solit, D.B., 2013. Tumor adaptation and resistance to RAF inhibitors. Nat. Med. 19, 1401–1409.

Liu, J., Chen, C., Wei, T., Gayet, O., Loncle, C., Borge, L., Dusetti, N., Ma, X., Marson, D., Laurini, E., Pricl, S., Gu, Z., Iovanna, J., Peng, L., Liang, X.-.J., 2021. Dendrimeric nanosystem consistently circumvents heterogeneous drug response and resistance in pancreatic cancer. Exploration 1, 21–34.

Liu, X., Wu, J., Yammine, M., Zhou, J., Posocco, P., Viel, S., Liu, C., Ziarelli, F., Fermeglia, M., Pricl, S., Victorero, G., Nguyen, C., Erbacher, P., Behr, J.-.P., Peng, L., 2011. Structurally flexible triethanolamine core PAMAM dendrimers are effective nanovectors for DNA transfection *in vitro* and *in vivo* to the mouse thymus. Bioconjug. Chem. 22, 2461–2473.

Liu, X., Zhou, J., Yu, T., Chen, C., Cheng, Q., Sengupta, K., Huang, Y., Li, H., Liu, C., Wang, Y., Posocco, P., Wang, M., Cui, Q., Giorgio, S., Fermeglia, M., Qu, F., Pricl, S., Shi, Y., Liang, Z., Rocchi, P., Rossi, J.J., Peng, L., 2014. Adaptive amphiphilic dendrimer-based nanoassemblies as robust and versatile siRNA delivery systems. Angew. Chem., Int. Ed. Engl. 53, 11822–11827.

Manalastas-Cantos, K., Konarev, P.V., Hajizadeh, N.R., Kikhney, A.G., Petoukhov, M.V., Molodenskiy, D.S., Panjkovich, A., Mertens, H.D.T., Gruzinov, A., Borges, C., Jeffries, C.M., Svergun, D.I., Franke, D., 2021. ATSAS 3.0: expanded functionality and new tools for small-angle scattering data analysis. J. Appl. Crystallogr. 54, 343–355.

Peppas, N.A., Sahlin, J.J., 1989. A simple equation for the description of solute release. III. Coupling of diffusion and relaxation. Int. J. .Pharm. 57, 169–172.

Pisarevsky, E., Blau, R., Epshtein, Y., Ben-Shushan, D., Eldar-Boock, A., Tiram, G., Koshrovski-Michael, S., Scomparin, A., Pozzi, S., Krivitsky, A., Shenbach-Koltin, G., Yeini, E., Fridrich, L., White, R., Satchi-Fainaro, R., 2020. Rational design of polyglutamic acid delivering an optimized combination of drugs targeting mutated BRAF and MEK in melanoma. Adv Ther (Weinh) 3, 2000028.

Raiteri, P., Laio, A., Gervasio, F.L., Micheletti, C., Parrinello, M., 2006. Efficient reconstruction of complex free energy landscapes by multiple walkers metadynamics. J. Phys. Chem. B 110, 3533.

Rheault, T.R., Stellwagen, J.C., Adjabeng, G.M., Hornberger, K.R., Petrov, K.G., Waterson, A.G., Dickerson, S.H., Mook Jr., R.A., Laquerre, S.G., King, A.J., Rossanese, O.W., Arnone, M.R., Smitheman, K.N., Kane-Carson, L.S., Han, C., Moorthy, G.S., Moss, K.G., Uehling, D.E., 2013. Discovery of dabrafenib: a selective inhibitor of Raf kinases with antitumor activity against B-Raf-driven tumors. ACS Med. Chem. Lett. 4, 358–362.

Ribas, A., Flaherty, K.T., 2011. BRAF targeted therapy changes the treatment paradigm in melanoma. Nat. Rev. Clin. Oncol. 8, 426–433.

Robert, C., Grob, J.J., Stroyakovskiy, D., Karaszewska, B., Hauschild, A., Levchenko, E., Chiarion Sileni, V., Schachter, J., Garbe, C., Bondarenko, I., Gogas, H., Mandalá, M., Haanen, J.B.A.G., Lebbé, C., Mackiewicz, A., Rutkowski, P., Nathan, P.D., Ribas, A., Davies, M.A., Flaherty, K.T., Burgess, P., Tan, M., Gasal, E., Voi, M., Schadendorf, D., Long, G.V., 2019. Five-year uutcomes with dabrafenib plus trametinib in metastatic melanoma. N. Engl. J. Med. 381, 626–636.

Roskoski, R., 2018. Targeting oncogenic Raf protein-serine/threonine kinases in human cancers. Pharmacol. Res. 135, 239–258.

Rossi, A., Roberto, M., Panebianco, M., Botticelli, A., Mazzuca, F., Marchetti, P., 2019. Drug resistance of BRAF-mutant melanoma: review of up-to-date mechanisms of action and promising targeted agents. Eur. J. Pharmacol. 862, 172621.

Russi, M., Cavalieri, G., Marson, D., Laurini, E., Pricl, S., 2022. Binding of the B-Raf inhibitors dabrafenib and vemurafenib to human serum albumin: a biophysical and molecular simulation study. Mol. Pharm. 19, 1619–1634.

Sjögren, E., Abrahamsson, B., Augustijns, P., Becker, D., Bolger, M.B., Brewster, M., Brouwers, J., Flanagan, T., Harwood, M., Heinen, C., Holm, R., Juretschke, H.P., Kubbinga, M., Lindahl, A., Lukacova, V., Münster, U., Neuhoff, S., Nguyen, M.A., Peer, A., Reppas, C., Hodjegan, A.R., Tannergren, C., Weitschies, W., Wilson, C., Zane, P., Lennernäs, H., Langguth, P., 2014. *In vivo* methods for drug absorption - comparative physiologies, model selection, correlations with *in vitro* methods (IVIVC), and applications for formulation/API/excipient characterization including food effects. Eur. J. Pharm. Sci. 57, 99–151.

Tangella, L.P., Clark, M.E., Gray, E.S., 2021. Resistance mechanisms to targeted therapy in BRAF-mutant melanoma - A mini review. Biochim. Biophys. Acta Gen. Subj. 1865, 129736.

Tian, Y., Guo, W., 2020. A Review of the molecular pathways involved in resistance to BRAF inhibitors in patients with advanced-stage melanoma. Med. Sci. Monit. 26, e920957.

Tsai, J., Lee, J.T., Wang, W., Zhang, J., Cho, H., Mamo, S., Bremer, R., Gillette, S., Kong, J., Haass, N.K., Sproesser, K., Li, L., Smalley, K.S., Fong, D., Zhu, Y.L., Marimuthu, A., Nguyen, H., Lam, B., Liu, J., Cheung, I., Rice, J., Suzuki, Y., Luu, C., Settachatgul, C., Shellooe, R., Cantwell, J., Kim, S.H., Schlessinger, J., Zhang, K.Y., West, B.L., Powell, B., Habets, G., Zhang, C., Ibrahim, P.N., Hirth, P., Artis, D.R., Herlyn, M., Bollag, G., 2008. Discovery of a selective inhibitor of oncogenic B-Raf kinase with potent antimelanoma activity. Proc. Natl. Acad. Sci. USA 105, 3041–3046.

Tsume, Y., Mudie, D.M., Langguth, P., Amidon, G.E., Amidon, G.L., 2014. The biopharmaceutics classification system: subclasses for *in vivo* predictive dissolution (IPD) methodology and IVIVC. Eur. J. Pharm. Sci. 57, 152–163.

Vanquelef, E., Simon, S., Marquant, G., Garcia, E., Klimerak, G., Delepine, J.C., Cieplak, P., Dupradeau, F.-.Y., 2011. R.E.D. Server: a web service for deriving RESP and ESP charges and building force field libraries for new molecules and molecular fragments. Nucleic Acids Res 39, W511–W517.

Vincent, K.M., Postovit, L.M., 2017. Investigating the utility of human melanoma cell lines as tumour models. Oncotarget 8, 10498–10509.

Wang, C., Ye, Y., Hochu, G.M., Sadeghifar, H., Gu, Z., 2016. Enhanced cancer immunotherapy by microneedle patch-assisted delivery of anti-PD1 antibody. Nano Lett 16, 2334–2340.

Wei, T., Chen, C., Liu, J., Liu, C., Posocco, P., Liu, X., Cheng, Q., Huo, S., Liang, Z., Fermeglia, M., Pricl, S., Liang, X.J., Rocchi, P., Peng, L., 2015. Anticancer drug nanomicelles formed by self-assembling amphiphilic dendrimer to combat cancer drug resistance. Proc. Natl. Acad. Sci. USA 112, 2978–2983.

Wei, T., Liu, J., Ma, H., Cheng, Q., Huang, Y., Zhao, J., Huo, S., Xue, X., Liang, Z., Liang, X.-.J., 2013. Functionalized nanoscale micelles improve drug delivery for cancer therapy *in vitro* and *in vivo*. Nano Lett 13, 2528–2534.

Weng, J., Tong, H.H.Y., Chow, S.F., 2020. *In vitro* release study of the polymeric drug nanoparticles: development and validation of a novel method. Pharmaceutics 12, 732.

Williams, P., 2005. 200 and More NMR experiments: a practical course, 3rd Edition Edited by S. Berger and S. Braun (University of Leipzig). Wiley-VCH, Weinheim, Germany.

Zhi, D., Yang, T., Zhang, T., Yang, M., Zhang, S., Donnelly, R.F., 2021. Microneedles for gene and drug delivery in skin cancer therapy. J. Control. Release 335, 158–177.